Super-Harmonic Imaging: Development of an Interleaved Phased-Array Transducer

Paul L. M. J. van Neer, *Student Member, IEEE*, Guillaume Matte, Mikhail G. Danilouchkine, Christian Prins, Franc van den Adel, and Nico de Jong, *Associate Member, IEEE*

***Abstract*—For several years, the standard in ultrasound imaging has been second-harmonic imaging. A new imaging technique dubbed "super-harmonic imaging" (SHI) was recently proposed. It takes advantage of the higher—third to fifth—harmonics arising from nonlinear propagation or ultrasound-contrast-agent (UCA) response. Next to its better suppression of near-field artifacts, tissue SHI is expected to improve axial and lateral resolutions resulting in clearer images than second-harmonic imaging. When SHI is used in combination with UCAs, a better contrast-to-tissue ratio can be obtained. The use of SHI implies a large dynamic range and requires a sufficiently sensitive array over a frequency range from the transmission frequency up to its fifth harmonic (bandwidth > 130%). In this paper, we present the characteristics and performance of a new interleaved dual frequency array built chiefly for SHI. We report the rationale behind the design choice, frequencies, aperture, and piezomaterials used. The array is efficient both in transmission and reception with well-behaved transfer functions and a combined −6-dB bandwidth of 144%. In addition, there is virtually no contamination of the harmonic components by spurious transducer transmission, due to low element-to-element crosstalk (< 30 dB) and a low transmission efficiency of the odd harmonics (< 46 dB). The interleaved array presented in this article possesses ideal characteristics for SHI and is suitable for other methods like second-harmonic, subharmonic, and second-order ultrasound field (SURF) imaging.**

I. Introduction

A decade ago it became possible to improve ultrasound image quality by exploiting the nonlinear nature of wave propagation. The technique is called tissue second-harmonic imaging and is based on the selective imaging of the second-harmonic frequency. Compared with fundamental imaging, second-harmonic imaging has a higher resolution and is less sensitive to near field artifacts, clutter, and off-axis scatterers [1]. As a result, second-harmonic imaging has been the standard in tissue imaging for several years. Nonlinear effects are not just exploited in tissue imaging. In fact, the selective imaging of the second-harmonic band was originally intended for ultrasound contrast agent (UCA) enhanced imaging [1]. Used in this way, the technique improved the contrast-to-tissue ratio (CTR) compared with fundamental imaging, thus enabling better imaging of blood flow [2].

Several other methods have been proposed to exploit the nonlinear behavior of UCAs. A new and promising imaging modality for the nondestructive imaging of UCAs is subharmonic imaging [3]–[6]. This imaging method is primarily intended to estimate blood perfusion by accurately quantifying the refresh of UCAs in a vascular bed after UCA destruction [4]. The principal advantage of UCA subharmonic imaging compared with UCA (second) harmonic imaging is that subharmonic signals are not generated in tissue at diagnostic pressures and frequencies maintaining a high CTR [5]. The optimal subharmonic imaging technique described in literature insonifies the UCA using a low-pressure excitation pulse—that is still higher than the UCA pressure threshold for subharmonics—at twice the UCA's resonance frequency [4].

Another promising UCA imaging modality utilizing nonlinear UCA behavior is second-order ultrasound field (SURF) imaging or radial modulation imaging. In this method, a low-frequency low-pressure pulse is transmitted (0.5–2 MHz), which manipulates the contrast agent around resonance by altering its scattering properties. In conjunction with the low-frequency pulse, a high-frequency pulse (3–14 MHz) is transmitted to detect the changes in scattering [7], [8]. The main advantage of this imaging technique is that it allows for UCA detection at clinically high frequencies—higher frequencies than the resonant frequencies of the UCAs. Example in-vivo B-mode results were presented by Masoy *et al.* [7], who obtained contrast-enhanced images of pig kidneys with a CTR of 15 to 40 dB.

Recently, a new imaging modality dubbed "super-harmonic imaging" (SHI) was proposed. The modality improves on second-harmonic imaging by combining the third to fifth harmonics arising from nonlinear wave propagation or contrast-agent response [2]. Tissue SHI efficiently suppresses near-field artifacts, reverberations, and off-axis artifacts in addition to the enhanced lateral and axial resolution. The resulting images showed more details than those produced by second-harmonic imaging [1]. Recently, this was confirmed in simulations and in-vitro experiments conducted by Ma *et al.* [9]. SHI is also promising for UCA-enhanced imaging. It has been demonstrated by Bouakaz *et al.* [2] that the CTR increases as a function of the order of the harmonic frequency. Thus, SHI in combination with contrast agents produces a

Manuscript received July 15, 2009; accepted November 10, 2009. The authors would like to express gratitude to SenterNovem for the financial support for project ISO52008.

P. L. M. J. van Neer is with the Department of Biomedical Engineering, Erasmus Medical Centre, Rotterdam, The Netherlands (e-mail: p.vanneer@erasmusmc.nl).

G. Matte, M. Danilouchkine, and N. de Jong are with the Department of Biomedical Engineering, Erasmus Medical Centre, Rotterdam, The Netherlands.

C. Prins and F. van den Adel are with Oldelft Ultrasound, Delft, The Netherlands.

Digital Object Identifier 10.1109/TUFFC.2010.1426

higher CTR than second-harmonic imaging, while at the same time minimizing shadowing effects. Until now, imaging with harmonics higher than the second one has been hampered by SNR issues, due to the progressively lower energy content of these harmonics.

A traditional phased-array design is inadequate for the implementation of the above imaging modalities. In the case of SHI, the principle of transmission at the fundamental and receiving the third to fifth harmonic implies a −6-dB bandwidth > 130%, a considerably larger bandwidth than that achievable with a conventional array configuration. Although −6-dB bandwidths as high as 140% are reported in the literature for single-element transducers made from a 1–3 single crystal-epoxy composite, the actual peak bandwidth at −6 dB reported for single crystal arrays are in the order of 95% [10]–[12], which is not sufficient for SHI. Next to the bandwidth demand, the implementation of SHI requires an array to be efficient in transmission—to generate significant higher harmonics—and sensitive in reception, as the reflected harmonic energy will be low.

This paper presents the rationale behind, construction of, and performance measurements of a very broadband array primarily intended for both tissue- and UCA-enhanced cardiac medical imaging. The array is mainly optimized for SHI, but is also capable of regular second-harmonic imaging. Furthermore, the suitability of the array for UCA techniques such as subharmonic and SURF imaging is discussed.

II. The Design

A. Requirements

The requirements for the new array can be listed as follows:

1) Very broad bandwidth. For SHI, the principle of transmission at the fundamental and receiving the third to fifth harmonic implies a −6-dB bandwidth > 130%.
2) High efficiency in transmission. For optimal image quality in the cases of tissue SHI and second-harmonic imaging, the peak pressure at focus should be as close as possible to the 1.9-MI limit allowed by the FDA.
3) High sensitivity in reception. In the case of the imaging modalities based on harmonics, the amplitude of the reflected signal at higher harmonic frequencies will be low for both nonlinear propagation and UCA-produced harmonics. Noise levels of ultrasound imaging systems are generally in the order of 10 μV_{rms}, thus, a receive sensitivity of ∼10 μV/Pa is required.
4) Have a good acoustic field with grating lobes of acceptably low amplitude. Cobbold [13] states that grating lobe levels should be 30 to 40 dB below the central lobe response at the receiving frequency of interest.

The main application of the array will be echocardiography, which adds the following requirements:

1) A small enough footprint to facilitate imaging through the ribs. Generally cardiac transducers have a footprint of about 15 × 15 mm.
2) Be optimized for an imaging depth of 0.5 to 15 cm.

B. Design Options

Several designs meet the bandwidth requirement for SHI [2, [14]–[22]. In the following paragraphs, we list these alternatives and consider their advantages and disadvantages.

The first option is to stack 2 active layers (usually PZT or a PZT composite) with different resonance frequencies on top of each other for each array element [14]–[17]. Advantages of this configuration are a limited total footprint of the array and ease of manufacture. Its main disadvantage is the electromechanical coupling between both active layers. This causes troughs in the frequency response of the transducer, if the resonance frequencies of both active elements are close to each other. Hossack *et al.* [14] presented a study on a transducer design consisting of a piezoelectric layer and an active (piezoelectric) matching layer. A proper adjustment of the phase response of the active matching layer and the subsequent addition of the responses of both active layers yielded a well-behaved broadband transfer function. Zhou *et al.* [15] showed in a finite element analysis study that the transfer function of a dual active layer transducer could be improved further with matched filtering. However, fairly complicated electronics [14], [16] and knowledge of the phase transfer function of each element are required for successful implementation. Also, the choice of matching layer characteristics is not straightforward, because the active layer used in transmission has a significantly different resonance frequency than the layer used in reception.

A second alternative was reported by Akiyama *et al.* [17]. They presented an ultra broadband transducer used in a mechanical sector scanner. The design features a PZT layer for transmission and a PVDF layer for reception. The PVDF layer functions well below its resonance frequency to guarantee electromechanical decoupling. However, the absolute sensitivity of PVDF applied in this manner is generally low.

The third option is a horizontal stack topology, where 2 low-frequency arrays are positioned laterally on both sides of a central high-frequency array [18]. The main advantage of this design is that the initial performance of each subarray is not modified. Disadvantages are the limited overlap of both acoustic beams and the increased footprint in the elevation dimension relative to a regular array design.

The fourth alternative is an interleaved configuration as proposed by Bouakaz *et al.* [2], [22], where the even elements are used in transmission and the odd elements are used in reception. The main advantages of this design are

the full overlap of the transmission and receive beams and a small footprint. Disadvantages are its relatively complicated manufacture and its intrinsically reduced sensitivity, because only half the elements are used in reception, which is necessary to keep the footprint size limited.

A final option is capacitive micromachined ultrasound transducers (cMUTs). cMUT transducers with −6-dB bandwidths of 130% have been reported in literature [19], [20]. However, cMUTs are held back by challenges such as achieving high output pressures [21], their inherent nonlinearity, and relatively high crosstalk [19]. One of the most important difficulties of cMUT technology is the contradictory requirement regarding the gap height to get both a high sensitivity in reception and a high output pressure in transmission [21]. Mills reported pulse-echo gains of cMUT transducers, which were between 10 and 20 dB less than a comparative PZT transducer [20].

After careful consideration of the advantages and disadvantages of each option, the interleaved design is chosen. Next to obvious advantages such as fully overlapping beams and a low footprint, there are no fundamental problems associated with this design. There is no direct electromechanical coupling between the elements, because the acoustic stacks for transmission and reception including the associated circuitry are fully separated. Also, the use of piezoceramics, such as PZT, single crystal, or piezocomposites, ensures the linear operation regime, even at high output pressures. In this way, any transmission of harmonics due to device nonlinearity, which considerably reduces the dynamic range of the imaging system, can be prevented. This fact is particularly important for SHI, because the level of higher harmonics generated by either nonlinear propagation or UCA response will be low.

The design does have an intrinsically reduced sensitivity in reception. However, this is alleviated by the fact that—like all designs with completely separate active elements for transmission and reception—each element can be acoustically matched and electrically tuned for its specific role.

C. Frequency

After selecting a design, the transmission frequency has to be chosen. This frequency influences other characteristics of the array, such as the receive frequency, layer thicknesses, and element dimensions.

For fundamental imaging, the transmission frequency used in clinical echocardiography is ∼3.5 MHz [23]. For both tissue- and UCA-enhanced second-harmonic imaging, the fundamental transmission frequency used in clinical echocardiography ranges between 1.6 and 1.8 MHz [23]. It is expected that for tissue SHI, the transmission frequencies will be lower still. The optimal transmission frequency for tissue SHI is intrinsically dependent on the level of the third to fifth harmonics at distances typical for cardiac imaging. Consequently, the level of these harmonics is determined by 2 competing phenomena: nonlinear propagation and attenuation. To find the optimal transmission frequency for SHI, we used a combination of nonlinear and linear simulations. Forward propagation was simulated using the Burgers equation, which describes the propagation of finite-amplitude plane progressive waves. The solution was found as a complex Fourier series using the iterative computation scheme given by Cobbold [13]. The back propagation was assumed to be linear. The acoustic nonlinearity parameter (B/A) was taken to be 5.8, and the attenuation was modeled as $\alpha = a.f^b$ with $a = 0.52$ dB cm^{-1} MHz$^{-\mathrm{b}}$ and $b = 1$. Furthermore, a density of 1060 kg/m^3 and an acoustic wavespeed of 1529 m/s were used. These values were reported for human fetal or dog cardiac tissue [24]. Calculations were performed for transmit frequencies between 0.5 and 1.8 MHz. The initial MI was kept at 1.5. The imaging depth was taken between 0.5 and 15 cm. The intensities of the first 5 harmonics and the super-harmonic versus the transmission frequency are shown in Fig. 1 for an imaging depth of 10 cm. The simulations showed that the frequency giving the optimal compromise between the rapidity of the build-up of harmonics at short distances and the attenuation of the harmonics at large distances was ∼1 MHz. This frequency was chosen as the resonance frequency of the low-frequency subarray. Correspondingly, a resonance frequency of ∼4 MHz was opted for the high-frequency subarray.

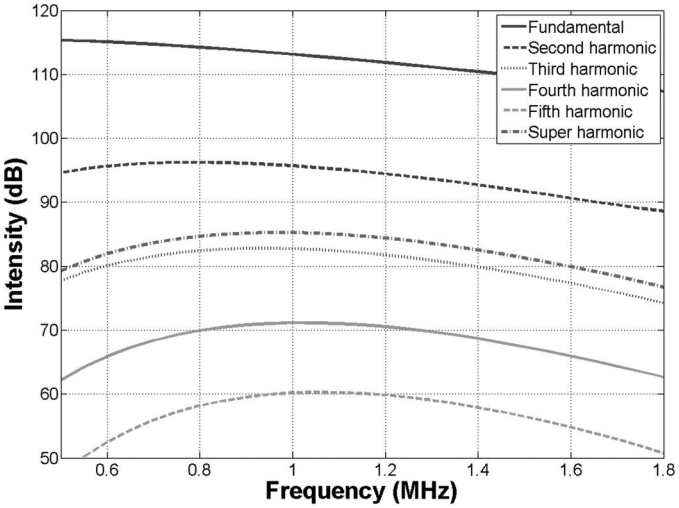

Fig. 1. The intensity of the first 5 harmonics and the super-harmonic versus the transmission frequency at an image depth of 10 cm. The intensity values are relative to 1 Pa. The forward propagation is modeled using the Burgers equation; the back propagation is assumed to be linear. The acoustic nonlinearity parameter (B/A) was 5.8 and the attenuation was modeled as $\alpha = a.f^b$ with $a = 0.52$ dB cm^{-1} MHz^{-b} and $b = 1$. The density was 1060 kg/m^3 and the acoustic wavespeed 1529 m/s. The initial MI was 1.5.

The optimal frequency for tissue SHI generally agrees with the requirements for UCA-enhanced SHI, because the UCAs used for cardiac applications are resonant at 1 to 5 MHz [25]. More specifically, SonoVue (Bracco Diagnostics Inc., Milan, Italy) and Definity/Luminity (Bristol-Myers Squibb, New York, New York) have reported resonance frequencies in the range of 1.5 to 3.1 MHz [7].

D. Element Geometry

The next feature to be established is the geometry of the 2 subarrays. The number and size of the array elements have a profound effect on characteristics such as the acoustic wave field, but they also affect the ease of manufacture.

1) Elevation Dimension: The elevation dimension of the low-frequency subarray was chosen to be 16 mm. This value was small enough for the ultrasound beam to pass unimpeded between the ribs, but still as high as possible to optimize the energy transferred into the medium. Due to the method used to interleave the elements, the elevation size of the high frequency subarray was 13 mm.

2) Lateral Dimension: Kerf/Pitch: The spacing between the elements of the final interleaved array is a compromise between the desire to waste as little as possible of the footprint real estate and the ability to merge both subarrays reliably—a critical step in the production process. If the elements of improperly merged subarrays touch each other, the element transmit efficiency and receive sensitivity are suboptimal. Crosstalk levels are also increased. Practical experience showed that an interelement spacing of 50 μm was optimal.

The width of the elements for both subarrays was the same to facilitate the array production process. The principal compromise for the lateral element size/pitch is the desire to have an as high as possible pitch-to-kerf ratio, while still having acceptable grating lobe levels at the highest intended transmitting frequency for the tissue imaging modalities (which is 1.6 to 1.8 MHz for tissue second-harmonic imaging). The effects of grating lobes are less important for UCA imaging, because UCAs exhibit a very nonlinear pressure-dependent response at pressures above 50 to 100 kPa [26]. The FIELD II simulation program [27], [28] was used to evaluate the peak intensities of the fundamental grating lobe relative to the main beam versus the subarray pitch at transmission frequencies of 1.7 to 1.8 MHz and a steering angle of 35°. The element elevation size was 13 mm, and the geometric elevation focus was 6 cm. No lateral focus was applied. The simulations were performed using 3 cycle sine bursts, which were Gaussian apodized. The propagation medium was assumed to be lossless. The peak intensities of the second-harmonic grating lobe relative to the main second-harmonic beam were estimated from the fundamental levels using the Fubini solution for weakly shocked plane waves produced by a monofrequency source [13]. A graph detailing the peak intensities of the simulated grating lobe versus the subarray pitch is shown in Fig. 2. Note that the subarray pitch was twice the element width plus twice the 50-μm element spacing of the final interleaved array. A subarray pitch of 0.5 mm yields a lateral element size of 0.2 mm (Fig. 2). For this chosen pitch, the second-harmonic levels in the grating lobe were ∼−45 dB at 1.7 MHz, ∼−38 dB at 1.75 MHz, and ∼−33 dB at 1.8 MHz relative to the second harmonic of the main bundle. The positions of the grating lobes in these cases were −83°, −79°, and −77°, respectively. The obtained characteristics match the requirements for grating lob levels, which should at least be 30 to 40 dB below the central lobe response [13].

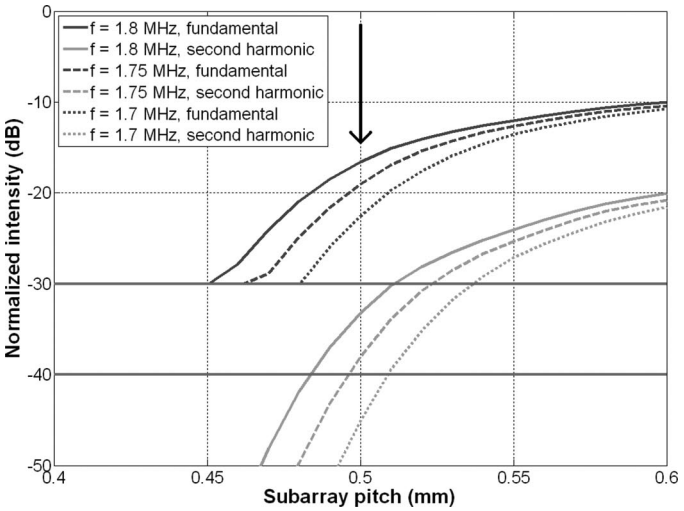

Fig. 2. The relation between the fundamental peak grating lobe intensity versus the subarray pitch, simulated using Field II. The grating lobe intensity was normalized by the main beam peak intensity. Note that the subarray pitch was double the element width plus double the 50-μm element spacing of the interleaved array. The peak second-harmonic intensity of the grating lobe was estimated from the fundamental using the Fubini solution. The simulations were performed using Gaussian apodized 3-cycle sine bursts at center frequencies of 1.7, 1.75, and 1.8 MHz. The element elevation size was 13 mm and the geometric elevation focus was 6 cm. The beam was unfocused in the lateral direction and steered 35°, the propagation medium was assumed to be lossless. The solid horizontal lines are at the intensity levels at which the grating lobe levels are low enough for high-quality imaging [13]. The subarray pitch used in the final interleaved array is indicated by the black arrow.

To keep the total footprint size practical, the final interleaved array consisted of a total of 88 elements, 44 of which were used in transmission and 44 were used in reception. This yielded a total footprint of 16 × 22 mm.

E. Choice of Piezomaterial

To optimize the receive sensitivity, research was conducted to select the optimal piezomaterial for an array with the selected frequency and aperture. After the piezomaterial was selected, the matching and backing materials were chosen to optimize each subarray for bandwidth.

A preselection of commercial piezomaterials was made by careful consideration of their datasheet properties and by using the KLM model [29]. Of these selected piezomaterials, custom arrays (18 elements, element size 13 × 0.2 mm, pitch 0.5 mm, resonance frequencies 3–4 MHz, backing 5.3 MRayl, no matching layers) were constructed to compare their performance in both transmission and reception. Columns 1 and 2 of Table I provide a summary of custom array characteristics. The arrays with large element variance were repoled in an attempt to improve performance. A voltage of 300 V DC was applied

TABLE I. CUSTOM-ARRAY AND FINAL INTERLEAVED-ARRAY CHARACTERISTICS.

	Custom array	Interleaved-array low-frequency subarray	Interleaved-array high-frequency subarray
Number of elements	18	44	44
Resonance frequency (MHz)	3–4	1	3.7
Element size (mm × mm)	13 × 0.2	16 × 0.2	13 × 0.2
Pitch (mm)	0.5	0.5	0.5
Piezomaterial	Various	CTS 3203HD	CTS 3203HD
Matching layers	—	1	2
Backing (MRayl)	5.3	3.2	3.2
Lens	—	Elevation, focus 6 cm	Elevation, focus 6 cm

TABLE II. CUSTOM-ARRAY PERFORMANCE PARAMETERS.

Custom array ID	Material type	Res. freq. (MHz)	Receive transfer Mean (μV/Pa)	Receive transfer Std. dev. (μV/Pa)	−6 dB bandwidth (%)	Transmit transfer Mean (kPa/V)	Transmit transfer Std. dev. (kPa/V)	Imp. at res. freq. Mag.	Imp. at res. freq. Phase (°)	SNR if receiving 1 Pa wave (dB)
1	CTS 3203HD	3.2	21	0.8	41	32.5	1	440	−18	24
2	Ferroperm Pz29	3.1	10.6	1.1	43	15.8	1.3	530	−36	16
3	Morgan PZT 5K.1	3.4	13.7	1.3	41	20.5	2.1	450	−22	17
4	TRS PZT HK.1HD	3.6	14.4	0.4	47	31.1	1.1	330	−17	18
5	CTS 50-50 composite	3.3	7	1.2	51	4.6	0.8	440	−77	14
6	CTS 60-40 composite	3.3	3.3	0.6	68	1.8	0.3	470	−86	3
7	Omega PZNT	1.6	15.6	3.8	48	5.5	1.8	850	−45	11
	after repoling:	2.0	15.6	3.7	45	7	2	800	−38	11
8	TRS PMN-30%PT	3.4	5.5	0.8	46	5.9	1.1	340	−50	18
	after repoling:	3.4	12.6	0.7	47	16	1.2	380	−35	15

over the element electrodes for about 30 min. This voltage was chosen to prevent overpoling of single crystal material and equals ∼700 V/mm.

The performance of the custom arrays was evaluated in terms of

- The maximal peak of the receive transfer function (shortened in this article as sensitivity) and the maximal peak of the transmit transfer function (shortened in this article as efficiency) of each element.
- The SNR. The SNR was determined for continuous ultrasound at the element's resonance frequency and a pressure of 1 Pa.

Table II summarizes the performance results of all 8 custom arrays. We consider the essential characteristics of each array, such as the resonance frequency, the mean and standard deviation of the sensitivity and efficiency, the −6-dB bandwidth, and the impedance and the SNR while receiving a 1-Pa pressure wave.

The custom array constructed of CTS 3203HD PZT was the most sensitive in our study, and this piezomaterial was used for the interleaved array.

A few remarks have to be made. In this study, no correction for differences in piezomaterial acoustic impedance was made, because preliminary calculations indicated that the correction factors were small compared with actual sensitivity differences—even when comparing composite piezomaterial to PZT. Also, the sensitivity as expressed in microvolts per Pascal is influenced by the resonance frequency of each array element. The resonance frequencies of the undiced slabs of piezomaterial lay between 4.0 to 4.9 MHz. However, KLM model simulations established that the effect of variation of the resonance frequency was less than 1 dB. Therefore, no correction was made for this effect.

The custom arrays based on composite piezomaterial had a somewhat low sensitivity. A retrospective investigation using an optical microscope showed damaged elements due to the dicing process. The arrays built using single crystal material had low mean sensitivities with high standard deviations and similar −6-dB bandwidths compared with PZT-based arrays—even after repoling. This was different from earlier studies, in which single crystal material was found to be superior in performance to PZT [10], [12], [30], [31]. Part of the explanation is that the array element height-to-width ratio was ∼2:1, which is not ideal for 33-mode vibrations. Also, the effects may be related to dicing difficulties. The custom arrays were diced using a diamond saw. A visual inspection using a microscope of the array elements showed that small chips had broken off the brittle single crystal material during dicing. Temperature-dependent degradation of the single crystal properties could not have been the cause, because the custom array production process takes place at low temperatures (below 70°C).

III. ARRAY PROTOTYPE

The transducer consisted of 2 interleaved subarrays with 88 transducer elements in total. The low- and high-

frequency elements were mechanically separated and electrically decoupled. That enabled the optimization of each element (e.g., matching layers, electrical tuning) for its specific role. Both the low- and high-frequency subarrays were built using CTS 3203HD piezomaterial. The subarray optimized for transmission had a resonance frequency of 1.0 MHz and consisted of 44 elements. The low-frequency elements had a single matching layer and a backing of 3.2 MRayl. The low frequency element size was 16 × 0.2 mm and the subarray had a pitch of 0.5 mm. The subarray optimized for reception had a resonance frequency of 3.7 MHz and was composed of 44 elements. The high-frequency elements had 2 matching layers on the front and a backing with an impedance of 3.2 MRayl. The high-frequency element size was 13 × 0.2 mm, and the subarray had a pitch of 0.5 mm. A lens with a geometric elevation focus at an axial distance of 6 cm was attached to the final interleaved transducer. The total footprint of the interleaved transducer was 16 × 22 mm. The electrical tuning of the final interleaved transducer to the imaging machine was optimized for SHI. A coil was mounted in series with each element of the low-frequency subarray, and a coil was fitted in parallel to each element of the high-frequency subarray.

Each subarray was constructed separately and cut with a diamond saw. The kerf between the elements was 0.3 mm for both subarrays. After cutting of the 2 subarrays, special tooling was used to merge the 2 subarrays, ensuring that the adjacent elements did not touch each other and aligning the front of both subarrays on the same plane.

The final interleaved transducer is shown schematically in Fig. 3. A summary of its characteristics is given in columns 3 and 4 of Table I. The transducer was manufactured by Oldelft Ultrasound, Delft, The Netherlands.

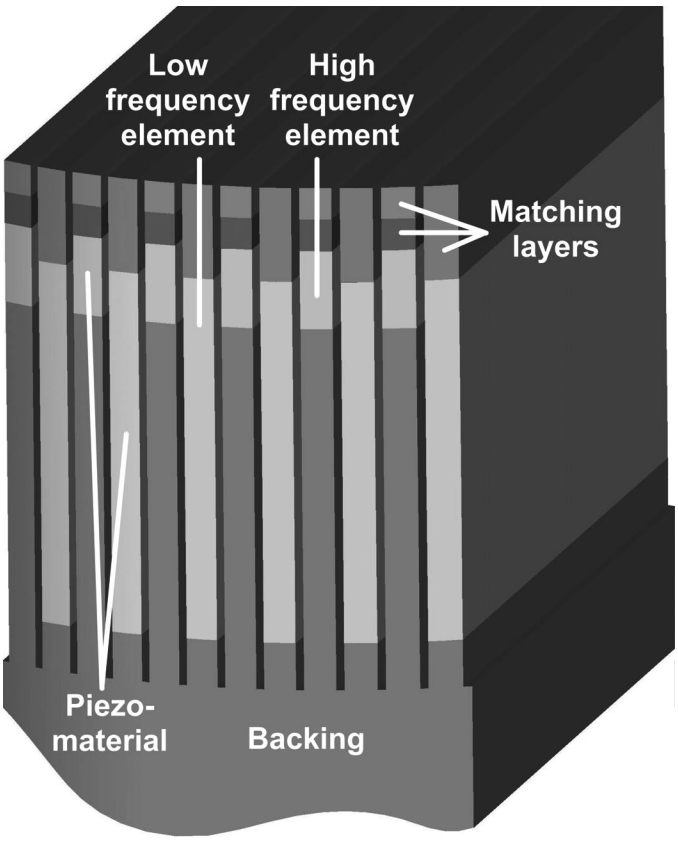

Fig. 3. Schematic showing the various parts of the final interleaved array.

IV. Acoustic Characterization

The final interleaved transducer was characterized by measuring its efficiency in transmission as well as its sensitivity in reception. For that, we determine the transmit-and-receive transfer functions of all the elements. Also, lateral and elevation beam profiles were measured at high-pressure ultrasound. Finally, the array's electrical and mechanical crosstalk was measured.

A. Transfer Functions

1) Definitions: The transducer transmit transfer function, $T_{\text{trans}}(\omega)$, is defined as

$$T_{\text{trans}}(\omega) = \frac{|p_0(\omega)|}{|V_T(\omega)|}, \tag{1}$$

with $p_0(\omega)$ the pressure at the transducer surface and $V_T(\omega)$ the voltage over the transducer electrodes.

The receive transfer function, $T_{\text{rec}}(\omega)$, is defined as

$$T_{\text{rec}}(\omega) = \frac{|V_{\text{T-open}}(\omega)|}{|p_a(\omega)|}, \tag{2}$$

with $V_{\text{T-open}}(\omega)$ the open circuit voltage over the transducer and $p_a(\omega)$ the pressure received on the transducer surface.

The transfer functions are calculated using the methods described in [32].

2) Setup: The experimental setup consisted of a water-filled tank. The array was attached to its sidewall. A calibrated source was mounted in a holder controlled by an *xyz*-system; see Fig. 4(a). The source was a flat circular piston transducer (V310, 2.25-MHz center frequency, diameter 6.35 mm, Panametrics, Waltham, MA).

For the transfer function measurements, the source was excited by an arbitrary waveform generator (33250A, Agilent, Loveland, CO), which produced 600 cycle sine bursts with an amplitude of 5 V. Each array element was connected to a computer-controlled matrix switch (custom built). The received signal was digitized by a digitizer card (DP235, Acqiris, Geneva, Switzerland) at a sampling rate of 100 MHz. The waveform generator was connected to a computer through GPIB, and the matrix switch was controlled using an Ethernet connection.

The acoustic pressures were low, so nonlinear propagation could be disregarded. Also attenuation was ig-

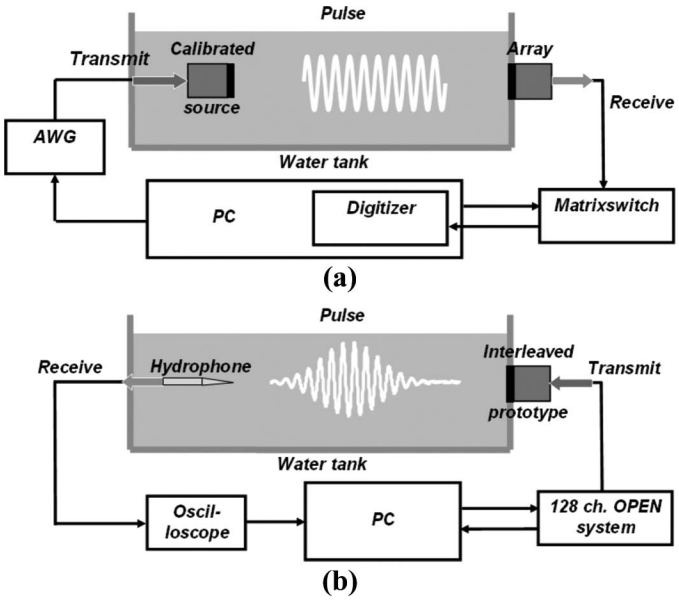

Fig. 4. (a) Setup to obtain transfer functions and SNR measurements and (b) setup to obtain beam profiles and crosstalk measurements.

nored, because the propagation distance in water was only ∼20 cm. The exact diffraction correction function posted by Goldstein *et al.* [33] was used to calculate on-axis pressures from the pressure produced at the source's surface. The elements of the high-frequency subarray were 13 mm long in the elevation direction. The spatial averaging correction factor, $S(\omega)$, was calculated by simulating the complete wave over the elevation range (−6.5 to 6.5 mm) produced by the calibrated source at the axial distance (∼23 cm) using Field II [27], [28] and calculating the mean pressure. $S(\omega)$ was recalculated for the elements of the low-frequency subarray, because their size was 16 × 0.2 mm.

B. Beam Profiles and Crosstalk Measurements

Beam profiles of the final interleaved array were measured with a hydrophone (diameter 0.2 mm, Precision Acoustics, Dorchester, UK) mounted in a xyz-system; see Fig. 4(b). The elements of the low-frequency subarray were excited by an 8-cycle Gaussian apodized sine burst at 1 MHz and amplitude of 60 V_{pp}, which was produced by a multichannel programmable ultrasound system (OPEN System, Lecoeur Electronique, Chuelles, France, first reported in [34]). The signals received by the hydrophone were digitized by an oscilloscope (9400A, Lecroy, Geneva, Switzerland) with a sampling frequency of 100 MHz and transferred to a computer for further processing.

The electrical and mechanical crosstalk was measured by exciting an element of either the low-frequency or the high-frequency subarray by a 3-cycle Gaussian apodized sine burst at the element's resonance with an amplitude of 12 V_{pp}. The response of all elements was measured and recalculated for the open circuit case ($V_{\text{resp}}^{\text{open}}$). The crosstalk was defined as

$$\text{Crosstalk} = 20 \cdot \log\left(\frac{V_{\text{resp}}^{\text{open}}}{V_{\text{excit}}}\right), \tag{3}$$

where V_{excit} is the excitation voltage, which is measured over the electrodes of the excited element.

V. Results: Interleaved Array Characteristics

A. Low-Frequency Subarray

The transmit-and-receive transfer functions of both the low- and high-frequency subarrays are shown in Fig. 5. The average efficiency (defined in this article as the maximum of the transmit transfer function) of the elements of the low-frequency subarray was ∼22 kPa/V; see Fig. 5(a). The average −10-dB bandwidth was 86%. After tuning, the average efficiency increased to ∼98 kPa/V; see Fig. 5(a). The −10-dB bandwidth was lowered from 86% to 55%. The transmit transfer function of the tuned elements shows that the efficiency of the third and fifth harmonics was, respectively, ∼46 dB and ∼55 dB below that of the fundamental.

Fig. 6 details the variation in element behavior by showing the normalized efficiency of the elements at resonance. The standard deviation of the normalized efficiency at resonance of the low-frequency subarray was ∼1.9 dB; see Fig. 6. The peak negative pressure reached ∼1.6 MPa at a focal distance of 6 cm, if the elements of the low-frequency subarray were excited with a 2-cycle 1-MHz Gaussian apodized sine burst of amplitude 120 V_{pp}. The peak negative pressure reached 2.0 MPa, if a similar excitation signal 3 cycles in length was applied.

In Fig. 7, the normalized time pulse at focus is displayed, which was produced by exciting the elements of the low-frequency subarray with a 2-cycle 1-MHz Gaussian apodized sine burst of amplitude 120 V_{pp}. The lateral focus of 6 cm was equal to the geometric elevation focus. The top panels show the fundamental and third-harmonic components; the lower panels detail the fourth and fifth harmonics. The fundamental −6-dB pressure pulse length was ∼2.9 μs at focus, and it decreased to 1.7, 1.4, and 1.3 μs for the third, fourth, and fifth harmonics, respectively. In Fig. 8(a), the lateral beam profiles of the fundamental up to the fifth harmonic recorded at a lateral focal distance of 6 cm (is equal to the geometric elevation focus) are presented. The lateral −6-dB beam width was 4.6, 2.6, 2.1, 1.7, and 1.5 mm for the fundamental, second, third, fourth, and fifth harmonic, respectively. In Fig. 8(b), lateral beam profiles of the second-, third-, and super-harmonic components are displayed. The super-harmonic component is defined as the combination of the third, fourth, and fifth harmonics. The −6-dB beam width of the super harmonic was 1.9 mm.

B. High-Frequency Subarray

The elements of the high-frequency subarray had an average sensitivity (defined in this article as the maxi-

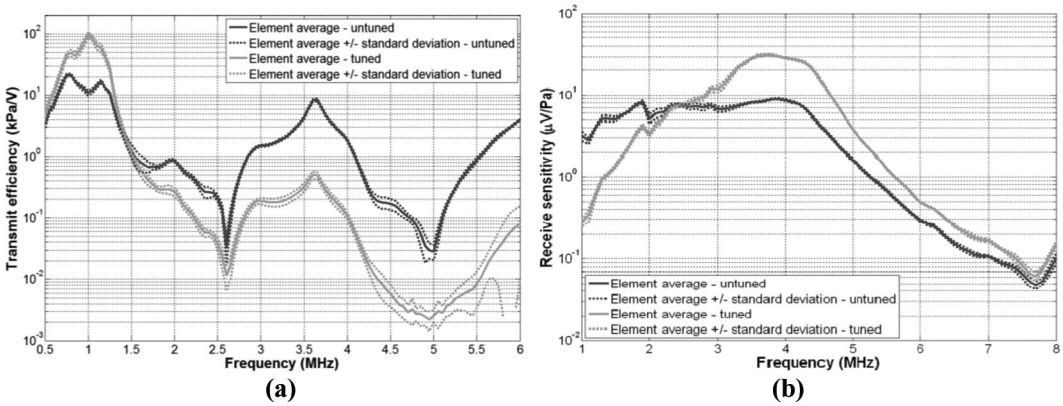

Fig. 5. (a) Transmit transfer function of the low-frequency subarray; the mean and standard deviations are based on measurements of 8 elements. (b) Receive transfer function of the high-frequency subarray; the mean and standard deviations are based on measurements of 8 elements.

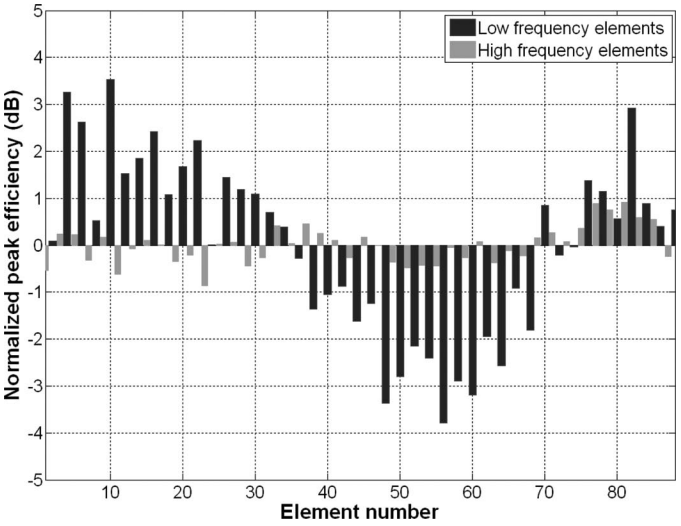

Fig. 6. The element variation of both subarrays by showing the efficiency (defined as the maximum of the transmit transfer function). The efficiency was normalized to the mean efficiency of either the low- or high-frequency subarray.

mum of the receive transfer function) of ∼9 μV/Pa, with a −10-dB bandwidth of 93%; see Fig. 5(b). After electrical tuning, the average sensitivity increased to ∼31 μV/Pa. The −10-dB bandwidth of the elements was lowered from 93% to 50%. The standard deviation of the normalized efficiency at resonance of the high-frequency part was ∼0.4 dB (Fig. 6). In transmission, the untuned elements of the high-frequency subarray had an average efficiency of ∼20 kPa/V.

C. Crosstalk

The inter-element crosstalk is shown in Fig. 9. Fig. 9(a) displays the crosstalk versus the element position relative to the excited element. The peak crosstalk amplitude was normalized by the excitation voltage. Fig. 9(b) shows the corresponding time delay. The mechanical crosstalk between the elements of the low-frequency subarray ranged from −53 to −31 dB relative to the transmitted signal, depending on the distance between the active element and the element of interest; see Fig. 9(a). Notice the local minimum in the mechanical crosstalk 3 elements away from the excited element; this was caused by diffraction effects in the backing. The large standard deviations of the 4 elements closest to the excited element in Figs. 9(a) and 9(b) were caused by overlap and interference of electrical and mechanical crosstalk. The large standard deviation in time delay of the excited element in Fig. 9(b) was caused by clipping of the receive circuitry. The mean element-to-element travel distance of the pressure wave was 0.8 mm, as was calculated from the mean relative time delay of 0.47 μs between the peak values of the mechanical crosstalk of each element; see Fig. 9(b). The crosstalk between the elements of the low-frequency subarray was not significant (< −60 dB) for elements further away than 10, except for elements at a distance of 16. In this case the crosstalk was ∼−37 dB with a standard deviation of 5.0 dB compared with the excitation signal. The time delay between the element and the excited element was 0 μs, implying purely electrical crosstalk. This crosstalk was explained by the wiring configuration.

Peak crosstalk from the low- to the high-frequency elements was ∼−60 dB relative to the transmitted signal with a standard deviation of 3.7 dB.

VI. Discussion

A. Performance of the Interleaved Array for SHI

The frequency response of the final interleaved array is shown in Fig. 10. Its combined −6-dB bandwidth exceeds 144%, whereas traditional arrays generally have 80% to 90% bandwidth. The graph summarizes the key characteristics of the implemented concept for the interleaved array in terms of bandwidth and efficiency.

The interleaved array consists of 2 separate subarrays, which are merged during manufacture. This is a critical step, and improperly merged arrays suffer from high crosstalk levels.

1) The Low-Frequency Subarray Used in Transmission: The resolution of a B-mode picture is determined by such

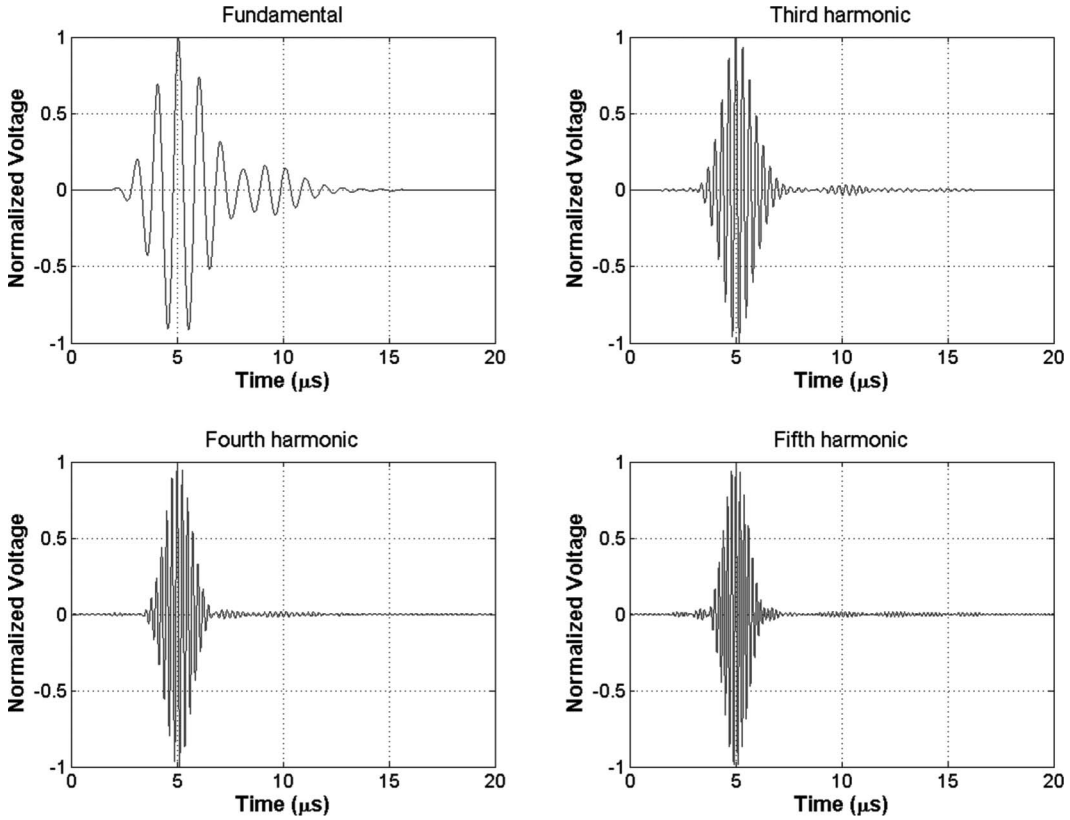

Fig. 7. The normalized fundamental, third-, fourth-, and fifth-harmonic components of a pressure signal recorded at focus. The lateral focus of 6 cm was equal to the geometric elevation focus. The elements of the low-frequency subarray were excited using a 2-cycle Gaussian apodized sine burst at 1 MHz with amplitude 120 V_{pp}.

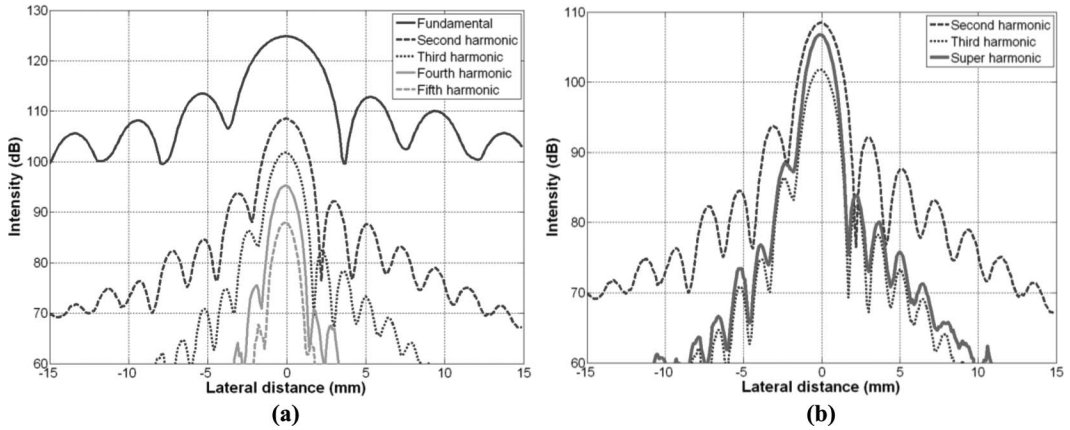

Fig. 8. (a) Lateral beam profiles of the fundamental up to the fifth harmonic at focus. The lateral focus of 6 cm was equal to the geometric elevation focus. The intensity values are relative to 1 Pa. The elements of the low-frequency subarray were excited using an 8-cycle Gaussian apodized sine burst at 1 MHz with amplitude 60 V_{pp}. (b) Zoomed lateral beam profiles of the second-, third-, and super-harmonic component at focus. The lateral focus of 6 cm was equal to the geometric elevation focus.

transmission beam characteristics as the length of the imaging pulse and the bundle profile. The effect of imaging schemes on the (axial) resolution is not treated, because it is considered to be out of the scope of this article.

The axial resolution is related to the time duration of the pressure pulses produced by the transducer (Fig. 7). Two main observations can be made. First, the pulse lengths of the third, fourth, and fifth harmonic are progressively shorter than the one of the fundamental. Second, the time trace of the fundamental is relatively long. This stems from the rather narrow bandwidth of the transmit transfer function of the tuned low frequency subarray (55% at −10 dB). Because of the intrinsic relation between the length of the fundamental pulse and the axial image resolution, it is highly desirable to increase the bandwidth. This goal can be achieved by either electrically tuning the low-frequency subarray off resonance or by use of a multiple resonance circuit. Both methods exchange transmit

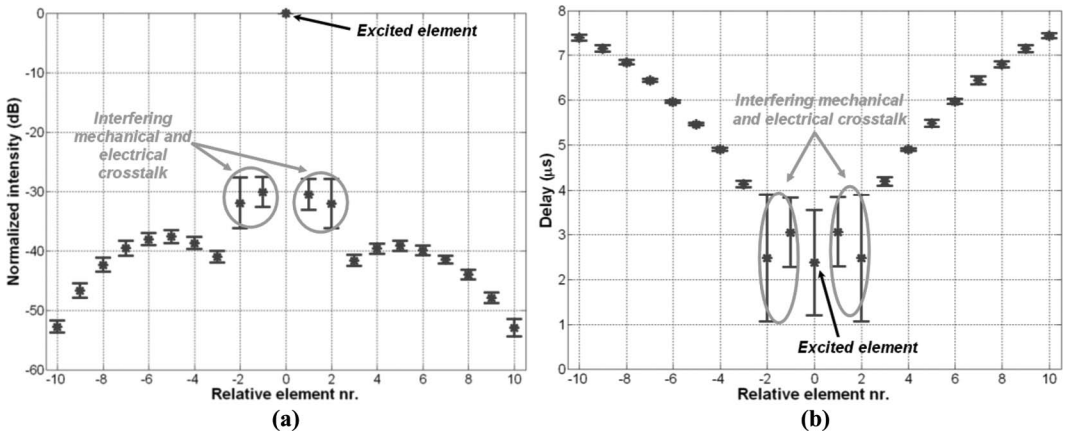

Fig. 9. (a) Peak element-to-element mechanical crosstalk of the low-frequency subarray relative to the excited element. The average and standard deviation are based on measurements of 9 elements. (b) Time delay of peak mechanical crosstalk of the low-frequency subarray relative to the excited element. The average and standard deviation are based on measurements of 9 elements.

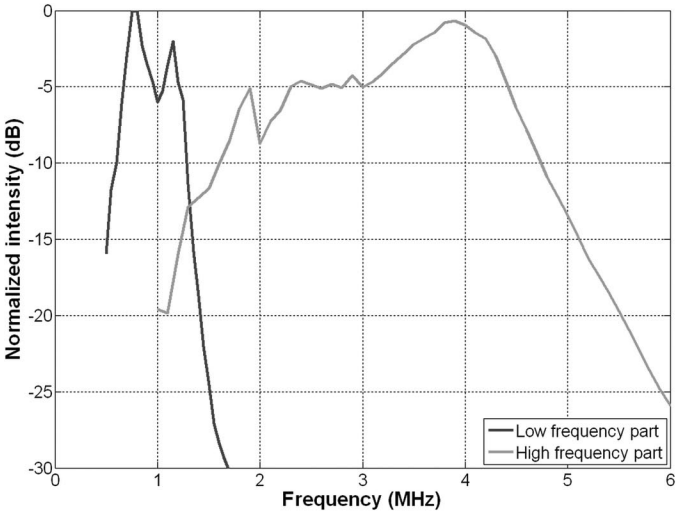

Fig. 10. The transmission transfer functions of the untuned low- and high-frequency subarrays combined to illustrate the interleaved array concept. The transfer functions are normalized by the peak transmission transfer of the low-frequency subarray.

efficiency for bandwidth, resulting in a lower peak pressure at focus—and, consequently, less energy in the higher harmonics—at the same excitation voltage. However, with the limited output voltage of our imaging system and a short excitation pulse of 2 cycles, the final interleaved array produced a maximum peak negative pressure of 1.6 MPa at focus. Because this is below the MI limit of 1.9, the electrical tuning was not optimized further for bandwidth.

The lateral resolution is best investigated using lateral beam profiles; see Fig. 8(a). The profiles show the progressively smaller −6-dB beam width of the higher harmonics. The most striking is the super-harmonic component shown in Fig. 8(b): its on-axis intensity is almost equal to the second harmonic, but it has an off-axis energy distribution similar to the third harmonic. This decreases the so-called haze in an image and by that improves the 2-D image quality. The −6-dB super-harmonic beam width is 59% smaller than the fundamental and 37% smaller than the second-harmonic beam width. Similar values were reported by Bouakaz *et al.* [1], who found the −6-dB beam width of the super-harmonic component to be 50% smaller than the fundamental and 30% smaller than the second harmonic in nonlinear wave propagation simulations of circular symmetric transducers. However, this comparison is not completely suitable. More appropriate would be to compare super-harmonic beam profiles to the optimal second-harmonic beam profiles produced using a transmission frequency of 1.6 to 1.8 MHz [23]. But the graph does demonstrate the potential of SHI, not only from a beam-width perspective but also because of the lower off-axis energy of the super-harmonic component at almost-equal-to-second-harmonic on-axis pressure intensity.

2) The High-Frequency Subarray Used in Reception: Next to the characteristics of the transmission beam, the image quality is further affected by the sensitivity of the subarray used in reception and the noise characteristics of the imaging system. The untuned elements of the high-frequency subarray had an average sensitivity of 9 μV/Pa, which is more than 50% less than that of the custom array made of the same piezomaterial (see Table II). This is caused by the extra attenuation of the lens on the array and the optimization for very wide bandwidth. The final interleaved array in combination with the OPEN system can detect a pressure as low as 3 Pa with 10-dB SNR. By far the largest noise contribution (17 μV_{RMS} over a 20-MHz band) originates from the OPEN system. To improve total system SNR, preamplifiers for each high-frequency element could be added in the handle. The necessary circuitry will be relatively simple, because no high-voltage protection circuitry is needed for the elements in SHI mode.

Currently, the electrical tuning of the final interleaved array is optimized for SHI. The high-frequency subarray is tuned on a single resonance, making the transducer plus circuitry quite narrowband (its −10-dB bandwidth is lowered from 93% to 50%). For SHI broadband electrical

tuning is preferable, such as using a matching circuit with multiple resonances distributed over the required pass band of 2.5 to 5.5 MHz. In both cases, the phase response of the matching circuit should be taken into account as well. In the future, programmable electrical tuning will be installed, yielding a transducer capable of efficient second-harmonic imaging and SHI.

3) Transducer-Generated SHI Contaminants: Because the energy of the super harmonics generated by either nonlinear propagation or UCA response is quite low, the contamination of the SHI component by transducer-produced signals at these frequencies should be minimized. For this, 2 transducer characteristics are essential. First, the low-frequency subarray should have a low efficiency at the super-harmonic frequencies. Second, the crosstalk between the low- and high-frequency subarrays should be minimized.

The transmit transfer function of the tuned low-frequency subarray showed that the third-harmonic efficiency was ~46 dB below its fundamental; see Fig. 4(a). The subarray's fifth-harmonic efficiency was more than 55 dB lower than its efficiency at the fundamental. By using a Gaussian modulated sine burst with a center frequency at the low-frequency elements' resonance with a −6-dB bandwidth similar to or slightly larger than the elements' fundamental band, the energy produced by the transducer at the third- or fifth-harmonic frequency can be kept < -100 dB. Thus, although the energy of the third- and fifth-harmonic components due to either nonlinear propagation or UCA response is quite low, the energy content of spuriously transmitted odd harmonics by the array is negligibly low.

Crosstalk from the low- to the high-frequency elements was ~−60 dB, due to the fact that the low- and high-frequency parts are in essence completely separate arrays. The high-frequency elements are quite insensitive at the frequencies generated by the low-frequency part during SHI and possible crosstalk artifacts in B-mode images are kept to a minimum.

The crosstalk between the low-frequency elements is important, because it has a detrimental influence on the transducer's ability to perform beam steering by effectively making the elements less omnidirectional. McKeighen [35] reported that crosstalk values of −30 dB are considered acceptable for most imaging situations. Crosstalk between low-frequency elements was < -31 dB, so the interleaved array performed superior to this value.

4) Abdominal SHI: SHI is also suitable for abdominal imaging. Because there is no size constraint on the array footprint in this application, the number of elements could be increased to 128; 64 elements used in transmission and 64 used in reception. In this case, the footprint size would be 16 × 32 mm instead of the current 16 × 22 mm. Advantages of this modification would be an increased maximum lateral focal distance (~10 cm instead of the current ~6 cm) and higher peak pressures at focus using equal excitation voltages. As the current interleaved array in conjunction with regular ultrasound equipment is already capable of reaching the 1.9-MI limit using a 3-cycle imaging burst, this means that the array's fundamental compromise between efficiency and bandwidth would shift more to bandwidth.

B. Potential Imaging Methods

The final interleaved array is suitable for new UCA imaging techniques such as subharmonic imaging or SURF imaging due to its broad bandwidth. The role of each subarray changes for these imaging techniques. For subharmonic imaging, the high-frequency elements are used in transmission and the low-frequency elements in reception. In the case of SURF imaging, both element types are used in transmission and reception. To facilitate these different roles, the electrical tuning has to be changed and optimized for each application. A possible problem is the existence of grating lobes produced when transmitting using the high-frequency elements. These grating lobes are caused by the fact that the subarray pitch of 0.5 mm is large relative to ultrasound wavelengths of 0.3 to 0.5 mm. For example, if a 4-MHz square wave is transmitted, a grating lobe of −10 dB relative to the main beam is located 45° off the main beam.

The following sections treat subharmonic and SURF imaging in combination with the final interleaved array, with the emphasis on usable imaging frequencies and grating lobes.

1) Subharmonic Imaging: First of all, the frequencies necessary for subharmonic imaging in cardiac applications are discussed in relation to the transfer function of the final interleaved array. Chomas *et al.* [4] report that the best subharmonic response is produced—while minimizing bubble instability—by using a transmission frequency that is twice the UCA's resonant frequency. UCAs used for cardiac applications are resonant at 1 to 5 MHz [25]. The final interleaved array is suitable for subharmonic imaging of UCAs with resonance frequencies between 1 and 2.4 MHz, because the high-frequency subarray is efficient up to ~4.8 MHz; see Fig. 10. Depending on the frequency of the subharmonic component, either the low- or high-frequency subarray should be used in reception.

The other topic of discussion is the influence of grating lobes. There exists an onset pressure threshold for the production of subharmonics by UCA. Below this threshold no subharmonic component can be detected. Chomas *et al.* [4] reported a pressure threshold of 200 kPa. By keeping the peak pressure in the grating lobe below this threshold, only the UCA in the main beam will produce significant subharmonic response. In this case, the existence of grating lobes can be disregarded. This implies that there is a frequency-dependent maximum of the peak pressure in the main beam. To study the aforementioned relation, we investigated the appearance of grating lobes in the acoustic field produced by the final interleaved array at varying

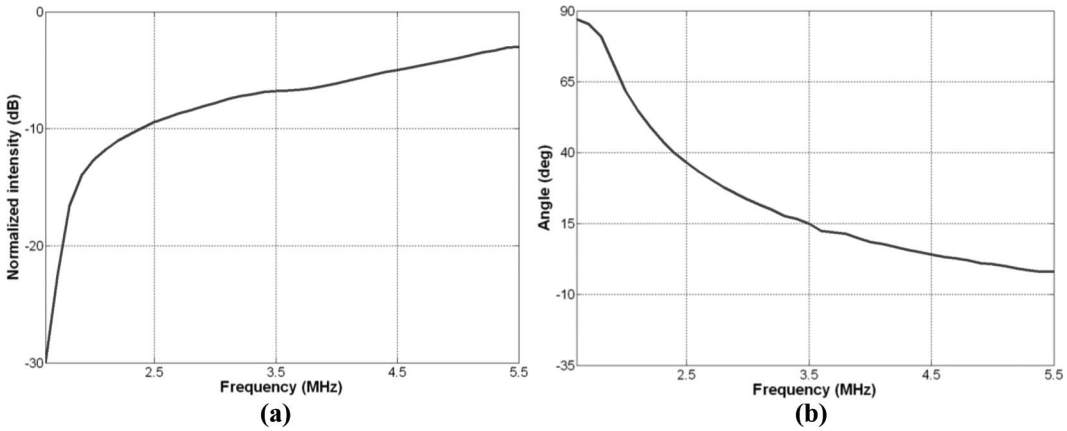

Fig. 11. (a) The relation between the fundamental peak grating lobe intensity versus the transmission frequency, simulated for the final interleaved array using Field II. The grating lobe intensity was normalized by the main fundamental beam peak intensity. The element size was 13 × 0.2 mm with a subarray pitch of 0.5 mm. The simulations were performed using 3-cycle sine bursts, which were Gaussian apodized. The geometric elevation focus of the beam was 6 cm; no lateral focus was applied. The beam was steered 35° and the propagation medium was assumed to be lossless. (b) The angle of the grating lobe versus transmission frequency. The beam was steered 35°.

transmission frequencies using the FIELD II simulation program [27], [28]. The element size was 13 × 0.2 mm with a subarray pitch of 0.5 mm. The simulations were performed using 3-cycle sine bursts that were Gaussian apodized. The geometric elevation focus of the beam was 6 cm, but no lateral focus was applied. The beam was steered 35°, and the propagation medium was assumed to be lossless. In Fig. 11(a), a graph is shown detailing the peak intensities of the simulated grating lobe versus the transmission frequency, and in Fig. 11(b), the angle of the grating lobe is shown versus the transmission frequency. It can be deduced from Fig. 11(a) that the maximum peak pressures of the main beam for subharmonic imaging reduce from 600 kPa at 2.5 MHz to 360 kPa at 4.5 MHz. These pressures are common for nondestructive UCA imaging. The actual pressure threshold value for the generation of subharmonics depends on the bubble type and the excitation frequency. Typical threshold values for free gas bubbles are around 60 kPa, if excited at twice the bubbles' resonance frequency [36]. For UCAs such as Levovist (Schering AG, Berlin, Germany), Optison (GE Healthcare, Chalfont St. Giles, UK), Definity, and Sonazoid (GE Healthcare, Chalfont St. Giles, UK), threshold values around 300 kPa were reported [37]. For SonoVue (Bracco Research, Geneva, Switzerland), the subharmonic pressure threshold was found to be 40 kPa [6].

2) SURF Imaging: First, the frequencies necessary for SURF imaging in cardiac applications in relation to the transfer function of the final interleaved array are discussed. Masoy *et al.* [7] state that the difference between the low- and high-frequency bursts should be on the order of 7 to 10 times for SURF imaging. In the case of echocardiography, that would imply a low-frequency pulse of ∼0.6 MHz and a high-frequency pulse of ∼4 to 5 MHz. The combined bandwidth of the interleaved array is sufficient for SURF imaging, albeit at relatively low frequencies. For example, if a manipulation pulse of 0.6 MHz is used, an imaging pulse of ∼4.2 MHz could be used. As the manipulation pulse pressures are usually in the order of 50 to 100 kPa [7], the normalized −10-dB transmit efficiency of the untuned low-frequency subarray at 0.6 MHz (Fig. 10) is sufficient.

Second, the effect of grating lobes on SURF imaging is discussed. It turns out that grating lobes caused by transmitting at higher frequencies are of minor importance for SURF imaging. Although the high-frequency imaging pulse (∼5 MHz) used in SURF would produce significant grating lobes, the low-frequency manipulation pulse (∼0.7 MHz) used to alter UCA scattering properties would not. Therefore, the final image subtraction step used in SURF imaging removes the UCA response from the grating lobes of the high-frequency imaging pulse.

3) Other Possibilities: Although the details are not covered in this article, the interleaved array is also suitable for other advanced imaging techniques. Examples are source prebiasing to reduce tissue harmonics in UCA imaging [38] or third-harmonic transmit phasing to either enhance the tissue second harmonic in tissue imaging or reduce the tissue second harmonic in UCA imaging [39].

VII. Conclusion

The interleaved array presented in this article possesses optimal characteristics for tissue and UCA-enhanced SHI. In addition, this array is suitable for a wide range of other experimental and clinical imaging modalities, such as second-harmonic, subharmonic, and SURF imaging.

With considerably less variation in response over the elements, much lower element-to-element crosstalk, a higher fundamental transmission efficiency, reduced third- and fifth-harmonic transmission efficiency, and improved sensitivity in reception, the interleaved array described in this article is a large improvement over the array reported by Bouakaz *et al.* [22] in 2004.

Acknowledgment

We would like to acknowledge the efforts of W. van Alphen, G. Springeling, J. M. G. Borsboom, C. Pakvis, J. E. T. van Wamel, J. G. Bosch, and T. R. Shrout.

References

[1] A. Bouakaz and N. de Jong, "Native tissue imaging at superharmonic frequencies," *IEEE Trans. Ultrason. Ferroelectr. Freq. Control*, vol. 50, no. 5, pp. 496–506, May 2003.

[2] A. Bouakaz, S. Frigstad, F. J. ten Cate, and N. de Jong, "Super harmonic imaging: A new imaging technique for improved contrast detection," *Ultrasound Med. Biol.*, vol. 28, no. 1, pp. 59–68, Jan. 2002.

[3] W. T. Shi and F. Forsberg, "Ultrasonic characterization of the nonlinear properties of contrast microbubbles," *Ultrasound Med. Biol.*, vol. 26, no. 1, pp. 93–104, Jan. 2000.

[4] J. Chomas, P. Dayton, D. May, and K. Ferrara, "Nondestructive subharmonic imaging," *IEEE Trans. Ultrason. Ferroelectr. Freq. Control*, vol. 49, no. 7, pp. 883–892, Jul. 2002.

[5] F. Forsberg, W. Shi, B. Jadidian, and A. Winder, "Multi-frequency harmonic arrays: Initial experience with a novel transducer concept for nonlinear contrast imaging," *Ultrasonics*, vol. 43, pp. 79–85, Dec. 2004.

[6] E. Biagi, L. Breschi, E. Vannacci, and L. Masotti, "Stable and transient subharmonic emissions from isolated contrast agent microbubbles," *IEEE Trans. Ultrason. Ferroelectr. Freq. Control*, vol. 54, no. 3, pp. 480–497, Mar. 2007.

[7] S. E. Masoy, O. Standal, P. Nasholm, T. F. Johansen, and B. Angelsen, "SURF imaging: *In vivo* demonstration of an ultrasound contrast agent detection technique," *IEEE Trans. Ultrason. Ferroelectr. Freq. Control*, vol. 55, no. 5, pp. 1112–1121, May 2008.

[8] H. H. Shariff, P. Bevan, R. Karshafian, R. Williams, and P. N. Burns, "Radial modulation imaging: Raising the frequency for contrast imaging," in *Proc. IEEE Ultrasonic Symp.*, Vancouver, Canada, 2006, pp. 104–107.

[9] Q. Ma, D. Zhang, X. Gong, and Y. Ma, "Investigation of superharmonic sound propagation and imaging in biological tissues *in vitro*," *J. Acoust. Soc. Am.*, vol. 119, no. 4, pp. 2518–2523, Apr. 2006.

[10] P. W. Rehrig, W. S. Hackenberger, and X. Jiang, "Status of piezoelectric single crystal growth for medical transducer applications," in *Proc. IEEE Ultrasonic Symp.*, Honolulu, HI, 2003, pp. 766–769.

[11] M. J. Zipparo, C. G. Oakley, D. M. Mills, A. M. Dentinger, and L. S. Smith, "A multirow single crystal phased array for wideband ultrasound imaging," in *Proc. IEEE Ultrasonic Symp.*, Montreal, Canada, 2004, pp. 1025–1029.

[12] H. Li, Y. C. Li, D. Zhou, J. Peng, H. S. Luo, and J. Y. Dai, "Application of PMNPT single crystal in a 3.2 MHz phased-array ultrasonic medical imaging transducer," in *Proc. IEEE Int. Symp. Applied Ferroelectrics*, Nara-city, Japan, 2007, pp. 572–574.

[13] R. S. C. Cobbold, *Foundations of Biomedical Ultrasound.* Oxford: Oxford University Press, 2007, pp. 227–251 and 437–438.

[14] J. A. Hossack and B. A. Auld, "Improving the characteristics of a transducer using multiple piezoelectric layers," *IEEE Trans. Ultrason. Ferroelectr. Freq. Control*, vol. 40, no. 2, pp. 131–139, Mar. 1993.

[15] S. Zhou and J. A. Hossack, "Investigation of digital filtering for stacked, phased ultrasound transducers," in *Proc. IEEE Ultrasonic Symp.*, Munich, Germany, 2002, pp. 1201–1204.

[16] J. A. Hossack, P. Mauchamp, and L. Ratsimandresey, "A high bandwidth transducer optimized for harmonic imaging," in *Proc. IEEE Ultrasonic Symp.*, San Juan, Puerto Rico, 2000, pp. 1021–1024.

[17] I. Akiyama, S. Saito, and A. Ohya, "Development of an ultra-broadband ultrasonic imaging system: Prototype mechanical sector device," *J. Med. Ultrasound*, vol. 33, no. 2, pp. 71–76, Jun. 2006.

[18] G. Ferin, M. Legros, N. Felix, C. Notard, and L. Ratsimandresey, "Ultra-wide bandwidth array for new imaging modalities," in *Proc. IEEE Ultrasonic Symp.*, New York, NY, 2007, pp. 204–207.

[19] S. Zhou, P. Reynolds, and J. A. Hossack, "Improving the performance of capacitive micromachined ultrasound transducers using modified membrane and support structures," in *Proc. IEEE Ultrasonic Symp.*, Rotterdam, The Netherlands, 2005, pp. 1925–1928.

[20] D. M. Mills, "Medical imaging with capacitive micromachined ultrasound transducer (cMUT) arrays," in *Proc. IEEE Ultrasonic Symp.*, Montreal, Canada, 2004, pp. 384–390.

[21] G. G. Yaralioglu, B. Bayram, and B. T. Khuri-Yakub, "Finite element analysis of CMUTs: Conventional vs. collapse operation modes," in *Proc. IEEE Ultrasonic Symp.*, Vancouver, Canada, 2006, pp. 586–589.

[22] A. Bouakaz, F. J. ten Cate, and N. de Jong, "A new ultrasonic transducer for improved contrast nonlinear imaging," *Phys. Med. Biol.*, vol. 49, no. 16, pp. 3515–3525, Aug. 2004.

[23] J. Kasprzak, B. Paelinck, F. Ten Cate, W. Vletter, N. De Jong, D. Poldermans, A. Elhendy, A. Bouakaz, and J. R. Roelandt, "Comparison of native and contrast-enhanced harmonic echocardiography for visualization of left ventricular endocardial border," *Am. J. Cardiol.*, vol. 83, no. 2, pp. 211–217, Jan. 1999.

[24] F. A. Duck, *Physical Properties of Tissues.* San Diego: Academic Press, Inc., 1990, pp. 80–139.

[25] P. Dawson, D. O. Cosgrove, and R. G. Grainger, *Textbook of Contrast Media*, Oxford: Isis Medical Media Ltd., 1999, pp. 480–485.

[26] M. Emmer, "The onset of bubble vibration," Ph.D. dissertation, Dept. Biomedical Technol., Erasmus Univ., Rotterdam, The Netherlands, 2009, p. 168.

[27] J. A. Jensen and N. B. Svendsen, "Calculation of pressure field from arbitrarily shaped, apodized and excited ultrasound transducers," *IEEE Trans. Ultrason. Ferroelectr. Freq. Control*, vol. 39, no. 2, pp. 262–267, Mar. 1992.

[28] J. A. Jensen, "Field: A program for simulating ultrasound systems," presented at the 10th Nordic-Baltic Conf. Biomedical Imaging, published in *Med. Biol. Eng. Comput.*, vol. 34, suppl. 1, part 1, pp. 351–353, 1996.

[29] D. A. Leedom, R. Krimholtz, and G. L. Matthaei, "Equivalent circuits for transducers having arbitrary even- or odd-symmetry piezoelectric excitation," *IEEE Trans. Sonics Ultrason.*, vol. SU-18, no. 3, pp. 128–141, Jul. 1971.

[30] S. M. Rhim and H. Jung, "Piezoelectric single crystal for medical ultrasound transducer," in *Proc. IEEE Ultrasonic Symp.*, New York, NY, 2007, pp. 300–304.

[31] S. M. Rhim, H. Jung, J. S. Jun, and J. S. Hwnag, "A 6.0 MHz 0.15 mm pitch phased array ultrasonic probe using PMN-PT single crystal," in *Proc. IEEE Ultrasonic Symp.*, Rotterdam, The Netherlands, 2005, pp. 219–222.

[32] P. L. M. J. van Neer, G. Matte, J. Sijl, J. M. G. Borsboom, and N. de Jong, "Transfer functions of US transducers for harmonic imaging and bubble responses," *Ultrasonics*, vol. 46, no. 4, pp. 336–340, Nov. 2007.

[33] A. Goldstein, D. R. Gandhi, and W. D. O'Brien, "Diffraction effects in hydrophone measurements," *IEEE Trans. Ultrason. Ferroelectr. Freq. Control*, vol. 45, no. 4, pp. 972–979, Jul. 1998.

[34] F. Vignon, J.-F. Aubry, M. Tanter, A. Margoum, M. Fink, and J. M. Lecoeur, "Dual-arrays brain imaging prototype: Experimental *in vitro* results," in *Proc. IEEE Ultrasonic Symp.*, Rotterdam, The Netherlands, 2005, pp. 504–507.

[35] R. E. McKeighen, "Design guildelines for medical ultrasonic arrays," in *Proc. SPIE*, San Diego, CA, 1998, pp. 2–18.

[36] A. Eller and H. Flynn, "Generation of subharmonic of the order one-half by bubbles in a sound field," *J. Acoust. Soc. Am.*, vol. 46, no. 3B, pp. 722–727, 1969.

[37] P. Frinking, E. Gaud, and M. Arditit, "Compression only behavior and subharmonic scattering of phospholipid-shell microbubbles," in *14th European Symp. Ultrasound Contrast Imaging (abstract)*, Rotterdam, The Netherlands, 2009, pp. 80–87.

[38] T. Christopher, "Source prebiasing for improved second harmonic bubble-response imaging," *IEEE Trans. Ultrason. Ferroelectr. Freq. Control*, vol. 46, no. 3, pp. 556–563, May 1999.

[39] C.-C. Shen, Y.-C. Wang, and Y.-C. Hsieh, "Third harmonic transmit phasing for tissue harmonic generation," *IEEE Trans. Ultrason. Ferroelectr. Freq. Control*, vol. 54, no. 7, pp. 1370–1381, Jul. 2007.

Paul L. M. J. van Neer was born in Heerlen, The Netherlands, in 1982. He earned the M.Sc. degree in biomedical technology at the Eindhoven University of Technology, Eindhoven, The Netherlands, in 2005. The same year he worked for the Signal Processing Systems Group, Department of Electrical Engineering, Eindhoven University of Technology on ultrasound contrast agent applications. In 2006, he joined the Department of Biomedical Engineering, Thorax Center, Erasmus

Medical Center, Rotterdam, The Netherlands. His current interests include transducer design, nonlinear ultrasound, tissue imaging methods, and ultrasound contrast agent imaging methods.

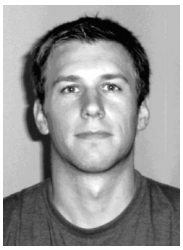

Guillaume Matte graduated from the University of Aix-Marseille III, Marseille, France. He received his M.S. degree in biomedical engineering in 2005 from the Ecole Supérieure d'Ingénieurs de Luminy. The same year he joined the department of biomedical engineering of the Thoraxcenter of Erasmus Medical Center, Rotterdam, The Netherlands. There he worked on nonlinear ultrasound for medical imaging techniques and transducer design. In 2008, he started to work for IXSEA, La Ciotat, France, as an acoustic engineer. His work focuses on electro-acoustic transducer design for underwater applications and nonlinear ultrasound applied to medical imaging.

Mikhail G. Danilouchkine was born in Ivanovo, former USSR, in 1969. He earned the M.Sc. degree (summa cum laude) in applied physics and mathematics from Moscow Institute for Physics and Technology, Moscow, Russia, in 1992. His Ph.D. study was successfully completed in the field of biophysics and bioelectromagnetism of the human heart from the same establishment in 1995. From 1995 till 1997, he was enrolled at the post-master program at Eindhoven University of Technology, Eindhoven, The Netherlands, and awarded a professional doctorate degree in engineering in computer science. Since 2005, he has been affiliated with the Department of Biomedical Engineering, Thorax Center, Erasmus Medical Center, Rotterdam, The Netherlands. His interests include signal and image processing, knowledge-guided segmentation and registration of medical images, visualization of scientific data, and tissue elasticity imaging.

Christian Prins was born in Rotterdam, The Netherlands, in 1977. He graduated from the Department of Applied Physics at the Technische Hoge School, Rijswijk, The Netherlands, in 2001. In 2001, he joined TNO-Fel, The Hague, The Netherlands, where he worked for one year on waveguide transitions. Since 2002, he has worked for Oldelft Ultrasound, Delft, The Netherlands, on acoustic transducer design.

Franc van den Adel was born in Dordrecht, The Netherlands, in 1959. He graduated from the Department of Applied Physics at the Technische Hoge School, Dordrecht, in 1982. In 1982, he started working at Oldelft Ultrasound, Delft, The Netherlands, on acoustic transducer design.

Nico de Jong graduated from Delft University of Technology, The Netherlands, in 1978. He got his M.Sc. degree in the field of pattern recognition. Since 1980, he has been a staff member of the Thoraxcenter of the Erasmus University Medical Center, Rotterdam, The Netherlands. At the Department of Biomedical Engineering, he developed linear and phased-array ultrasonic probes for medical diagnosis, especially compound and transesophageal transducers. In 1986, his interest in ultrasound applications shifted toward the theoretical and practical background of ultrasound contrast agents. In 1993, he received his Ph.D. degree for "Acoustic properties of ultrasound contrast agents." De Jong is the project leader of STW and FOM projects on ultrasound contrast imaging, molecular imaging, and drug delivery systems and participates with his group in several European projects. Since 1996, and together with Folkert ten Cate, MD, he has been the organizer of the annual European Symposium on Ultrasound Contrast Imaging held in Rotterdam and attended by approximately 175 scientists from all over the world.

Since 2003 Dr. de Jong has been part-time professor at the University of Twente, Twente, The Netherlands. He has published more than 100 scientific papers and has several patents on ultrasound contrast imaging and transducer design.